

Modelling the nebular emission from primeval to present-day star-forming galaxies

Julia Gutkin¹^{*}, Stéphane Charlot¹ and Gustavo Bruzual²

¹*Sorbonne Universités, UPMC-CNRS, UMR7095, Institut d’Astrophysique de Paris, F-75014, Paris, France*

²*Instituto de Radioastronomía y Astrofísica, UNAM, Campus Morelia, México*

Accepted XXX. Received YYY; in original form ZZZ

ABSTRACT

We present a new model of the nebular emission from star-forming galaxies in a wide range of chemical compositions, appropriate to interpret observations of galaxies at all cosmic epochs. The model relies on the combination of state-of-the-art stellar population synthesis and photoionization codes to describe the ensemble of H II regions and the diffuse gas ionized by young stars in a galaxy. A main feature of this model is the self-consistent yet versatile treatment of element abundances and depletion onto dust grains, which allows one to relate the observed nebular emission from a galaxy to both gas-phase and dust-phase metal enrichment. We show that this model can account for the rest-frame ultraviolet and optical emission-line properties of galaxies at different redshifts and find that ultraviolet emission lines are more sensitive than optical ones to parameters such as C/O abundance ratio, hydrogen gas density, dust-to-metal mass ratio and upper cutoff of the stellar initial mass function. We also find that, for gas-phase metallicities around solar to slightly sub-solar, widely used formulae to constrain oxygen ionic fractions and the C/O ratio from ultraviolet and optical emission-line luminosities are reasonable faithful. However, the recipes break down at non-solar metallicities, making them inappropriate to study chemically young galaxies. In such cases, a fully self-consistent model of the kind presented in this paper is required to interpret the observed nebular emission.

Key words: galaxies: general – galaxies: ISM – galaxies: abundances – galaxies: high-redshift

1 INTRODUCTION

The emission from interstellar gas heated by young stars in galaxies contains valuable clues about both the nature of these stars and the physical conditions in the interstellar medium (ISM). In particular, prominent optical emission lines produced by H II regions, diffuse ionized gas and a potential active galactic nucleus (AGN) in a galaxy are routinely used as global diagnostics of gas metallicity and excitation, dust content, star formation rate and nuclear activity (e.g., Izotov & Thuan 1999; Kobulnicky et al. 1999; Kauffmann et al. 2003; Nagao et al. 2006b; Kewley & Ellison 2008). Near-infrared spectroscopy enables such studies in the optical rest frame of galaxies out to redshifts $z \sim 1$ –3 (e.g., Pettini & Pagel 2004; Hainline et al. 2009; Richard et al. 2011; Guaita et al. 2013; Steidel et al. 2014; Shapley et al. 2015). While the future *James Webb Space Telescope* (*JWST*) will enable rest-frame optical emission-line studies

out to the epoch of cosmic reionization, rapid progress is being accomplished in the observation of fainter emission lines in the rest-frame ultraviolet spectra of galaxies in this redshift range (e.g., Shapley et al. 2003; Erb et al. 2010; Stark et al. 2014, 2015a,b, 2016; Sobral et al. 2015). The interpretation of these new observations requires the development of models optimised for studies of the ultraviolet – in addition to optical – nebular properties of chemically young galaxies, in which heavy-element abundances (for example, the C/O ratio; Erb et al. 2010; Cooke et al. 2011) are expected to differ substantially from those in star-forming galaxies at lower redshifts.

Several models have been proposed to compute the nebular emission of star-forming galaxies through the combination of a stellar population synthesis code with a photoionization code (e.g., Garcia-Vargas et al. 1995; Stasińska & Leitherer 1996; Charlot & Longhetti 2001, hereafter CL01; Zackrisson et al. 2001; Kewley & Dopita 2002; Panuzzo et al. 2003; Dopita et al. 2013; see also Anders & Fritze-v. Alvensleben 2003; Schaerer & de Barros 2009). These mod-

* E-mail: gutkin@iap.fr

els have proved valuable in exploiting observations of optical emission lines to constrain the young stellar content and ISM properties of star-forming galaxies (e.g., Brinchmann et al. 2004; Blanc et al. 2015). A limitation of current models of nebular emission is that these were generally calibrated using observations of H_{II} regions and galaxies in the nearby Universe, which increasingly appear as inappropriate to study the star formation and ISM conditions of chemically young galaxies (e.g., Erb et al. 2010; Steidel et al. 2014, 2016; Shapley et al. 2015; see also Brinchmann et al. 2008; Shirazi et al. 2014). We note that this limitation extends to chemical abundance estimates based on not only the so-called ‘strong-line’ method, but also the ‘direct’ (via the electronic temperature T_e) method, since both methods rely on the predictions of photoionization models (see Section 5). Another notable limitation of current popular models of the nebular emission from star-forming galaxies is that these do not incorporate important advances achieved over the past decade in the theories of stellar interiors (e.g., Eldridge et al. 2008; Bressan et al. 2012; Ekström et al. 2012; Georgy et al. 2013; Chen et al. 2015) and atmospheres (e.g., Hauschildt & Baron 1999; Hillier & Miller 1999; Pauldrach et al. 2001; Lanz & Hubeny 2003, 2007; Hamann & Gräfener 2004; Martins et al. 2005; Puls et al. 2005; Rodríguez-Merino et al. 2005; Leitherer et al. 2010).

In this paper, we present a new model of the ultraviolet and optical nebular emission from galaxies in a wide range of chemical compositions, appropriate to model and interpret observations of star-forming galaxies at all cosmic epochs. This model is based on the combination of the latest version of the Bruzual & Charlot (2003) stellar population synthesis code (Charlot & Bruzual, in preparation; which incorporates the stellar evolutionary tracks of Bressan et al. 2012; Chen et al. 2015 and the ultraviolet spectral libraries of Lanz & Hubeny 2003, 2007; Hamann & Gräfener 2004; Rodríguez-Merino et al. 2005; Leitherer et al. 2010) with the latest version of the photoionization code CLOUDY (c13.03; described in Ferland et al. 2013). We follow CL01 and use effective (i.e. galaxy-wide) parameters to describe the ensemble of H_{II} regions and the diffuse gas ionized by successive stellar generations in a galaxy. We take special care in parametrizing the abundances of heavy elements and their depletion onto dust grains in the ISM, which allows us to model in a self-consistent way the influence of ‘gas-phase’ and ‘interstellar’ (i.e. gas+dust-phase) abundances on emission-line properties. We build a comprehensive grid of models spanning wide ranges of interstellar parameters, for stellar populations with a Chabrier (2003) stellar initial mass function (IMF) with upper mass cutoffs 100 and 300 M_⊙. We show that these models can reproduce available observations of star-forming galaxies in several line-ratio diagrams at optical ([O II]λλ3726, 3729, H β , [O III]λ5007, H α , [N II]λ6584, [S II]λλ6717, 6731) and ultraviolet (N V λλ1238, 1242, C IV λλ1548, 1551, He II λ1640, O III]λ1666, [C III]λ1907+C III]λ1909, [Si III]λ1883+Si III]λ1892) wavelengths. We further exploit this model grid to quantify the limitations affecting standard recipes based on the direct- T_e method to measure element abundances from emission-line luminosities. The model presented in this paper has already been used successfully to interpret observations of high-redshift star-forming galaxies (Stark et al. 2014, 2015a,b, 2016) and to

define new ultraviolet and optical emission-line diagnostics of active versus inactive galaxies (Feltre et al. 2016).

We present our model in Section 2, where we parametrize the nebular emission of a star-forming galaxy in terms of stellar population, gas and dust parameters. In Section 3, we compute a large grid of photoionization models and show that these succeed in reproducing observations of galaxies from the Sloan Digital Sky Survey (SDSS) in standard optical line-ratio diagrams. We investigate the ultraviolet properties of these models and compare them with observations of star-forming galaxies at various cosmic epochs in Section 4. In Section 5, we investigate the limitations of standard recipes based on the direct- T_e method to measure element abundances from emission-line luminosities, focusing on the C/O ratio as a case study. We summarise our conclusions in Section 6.

2 MODELLING

To model the stellar and nebular emission from a star-forming galaxy, we adopt the isochrone synthesis technique introduced by Charlot & Bruzual (1991) and express the luminosity per unit wavelength λ emitted at time t as

$$L_\lambda(t) = \int_0^t dt' \psi(t - t') S_\lambda[t', Z(t - t')] T_\lambda(t, t'), \quad (1)$$

where $\psi(t - t')$ is the star formation rate at time $t - t'$, $S_\lambda[t', Z(t - t')]$ the luminosity produced per unit wavelength per unit mass by a single stellar generation of age t' and metallicity $Z(t - t')$ and $T_\lambda(t, t')$ the transmission function of the ISM, defined as the fraction of the radiation produced at wavelength λ at time t by a generation of stars of age t' that is transferred by the ISM. We describe below the prescriptions we adopt for the functions S_λ and T_λ in equation (1). We do not consider in this paper the potential contributions to $L_\lambda(t)$ by shocks nor an AGN component.

2.1 Stellar emission

We compute the spectral evolution of a single stellar generation $S_\lambda[t', Z(t - t')]$ in equation (1) above using the latest version of the Bruzual & Charlot (2003) stellar population synthesis model (Charlot & Bruzual, in preparation; see also Wofford et al. 2016). This incorporates stellar evolutionary tracks computed with the recent code of Bressan et al. (2012) for stars with initial masses up to 350 M_⊙ (Chen et al. 2015) and metallicities in the range $0.0001 \leq Z \leq 0.040$ (the present-day solar metallicity corresponding to $Z_\odot = 0.01524$; see also Section 2.3 below). These tracks include the evolution of the most massive stars losing their hydrogen envelope through the classical Wolf-Rayet phase (i.e., stars more massive than about 25 M_⊙ at $Z = Z_\odot$, this threshold increasing as metallicity decreases).

To compute the spectral energy distributions of stellar populations, the above evolutionary tracks are combined with different stellar spectral libraries covering different effective-temperature, luminosity-class and wavelength ranges (Pauldrach et al. 2001; Rauch 2002; Lanz & Hubeny 2003; Hamann & Gräfener 2004; Martins et al. 2005; Rodríguez-Merino et al. 2005; Sánchez-Blázquez et al. 2006;

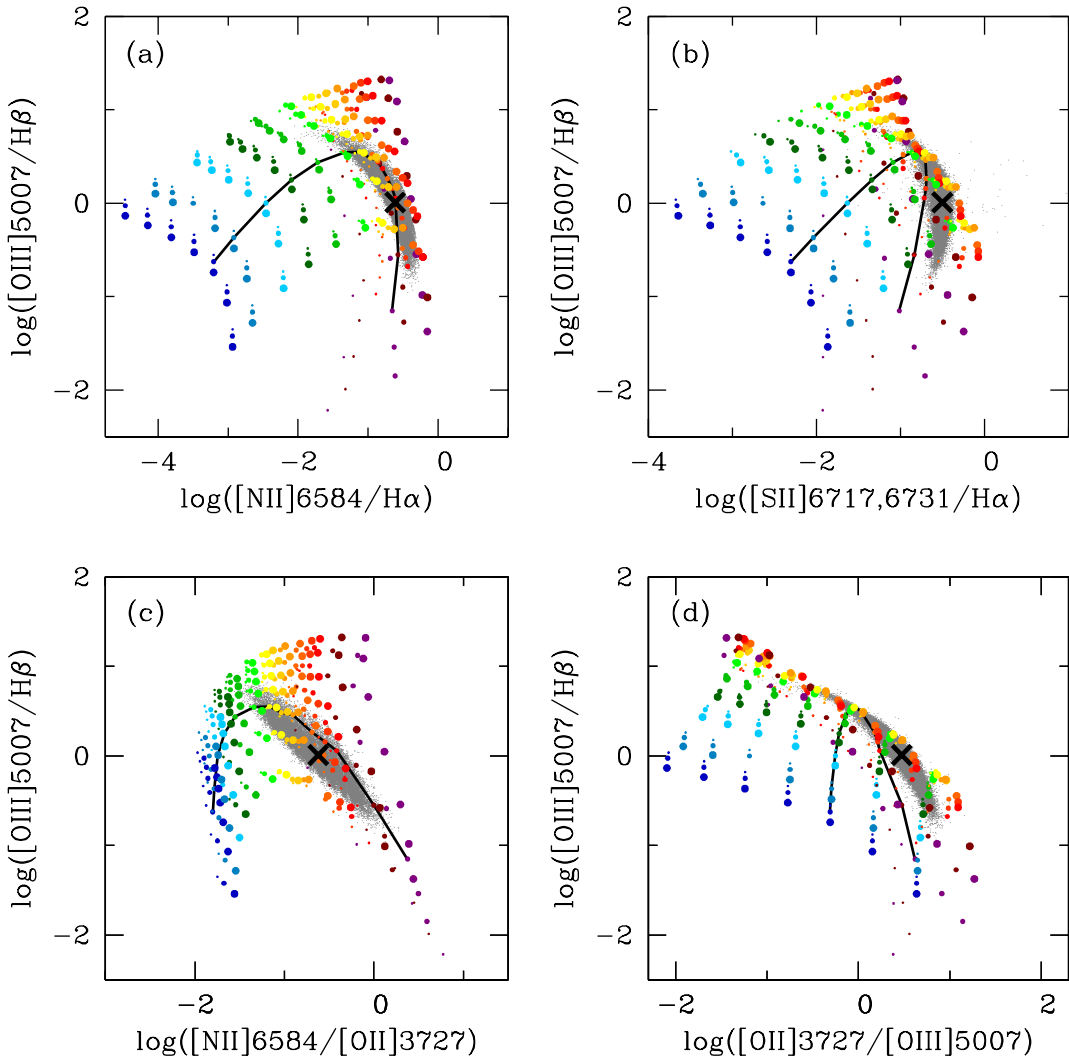


Figure 2. Luminosity ratios of prominent optical emission lines predicted by the photoionization models described in Section 2: (a) $[\text{O III}]\lambda 5007/\text{H}\beta$ against $[\text{N II}]\text{H}\alpha$; (b) $[\text{O III}]\lambda 5007/\text{H}\beta$ against $[\text{S II}]\lambda\lambda 6717, 6731/\text{H}\alpha$; (c) $[\text{O III}]\lambda 5007/\text{H}\beta$ against $[\text{N II}]\lambda 6584/[\text{O II}]\lambda 3727$; and (d) $[\text{O III}]\lambda 5007/\text{H}\beta$ against $[\text{O II}]\lambda 3727/[\text{O III}]\lambda 5007$. The models assume constant star formation over the past 100 Myr and fixed hydrogen density, $n_{\text{H}} = 100 \text{ cm}^{-3}$, carbon-to-oxygen ratio, $(\text{C}/\text{O})_{\odot}=0.44$, and IMF upper mass cutoff, $m_{\text{up}} = 100 \text{ M}_{\odot}$. They are shown for 14 interstellar metallicities in the range $0.0001 \leq Z_{\text{ISM}} \leq 0.040$ (colour-coded as in Fig. 1; see Table 2), 7 zero-age ionization parameters in the range $-4 \leq \log U_{\text{S}} \leq -1$, in bins of 0.5 dex (in order of increasing $[\text{O III}]/\text{H}\beta$ ratio at fixed metallicity), and 3 dust-to-metal mass ratios $\xi_{\text{d}} = 0.1, 0.3$ and 0.5 (in order of increasing symbol size). In each panel, a line links models with $\log U_{\text{S}} = -3.0$ at all metallicities, while the black cross shows the ‘standard’ model defined in Section 3.2. The grey dots show high-quality observations of star-forming galaxies from the SDSS DR7, corrected for attenuation by dust as described in Brinchmann et al. (2004).

abundance $12 + \log (\text{O/H})_{\text{gas}} = 8.70$, while the interstellar oxygen abundance is that corresponding to the metallicity $Z_{\text{ISM}} = 0.014$ in Table 2, i.e., $12 + \log \text{O/H} = 8.80$.

3.3 Influence of model parameters on optical emission-line properties

We now briefly describe the influence of the main adjustable parameters of our model on the predicted optical emission-line properties of star-forming galaxies (see also CL01). In this description, we explore the effect of varying a single parameter at a time, keeping the other main adjustable parameters fixed:

Interstellar metallicity. Fig. 2 (solid line) shows that increasing Z_{ISM} at fixed other parameters makes the $[\text{O III}]/\text{H}\beta$ ratio rise to a maximum (around $Z_{\text{ISM}} \approx 0.006$) and then decrease again. This is because gas cooling through collisionally excited optical transitions first increases as the abundance of metal coolants rises, until the electronic temperature drops low enough for cooling to become dominated by infrared fine-structure transitions (e.g., Spitzer 1978). Efficient fine-structure cooling by doubly-ionized species in the inner parts of H II regions also makes the $[\text{O II}]/[\text{O III}]$ ratio rise in Fig. 2d (Stasińska 1980). The $[\text{S II}]/\text{H}\alpha$ ratio behaves in a similar way to the $[\text{O III}]/\text{H}\beta$ ratio (Fig. 2b). In contrast, our inclusion of secondary nitrogen production causes the $[\text{N II}]/\text{H}\alpha$ and $[\text{N II}]/[\text{O II}]$ to rise steadily with metallicity

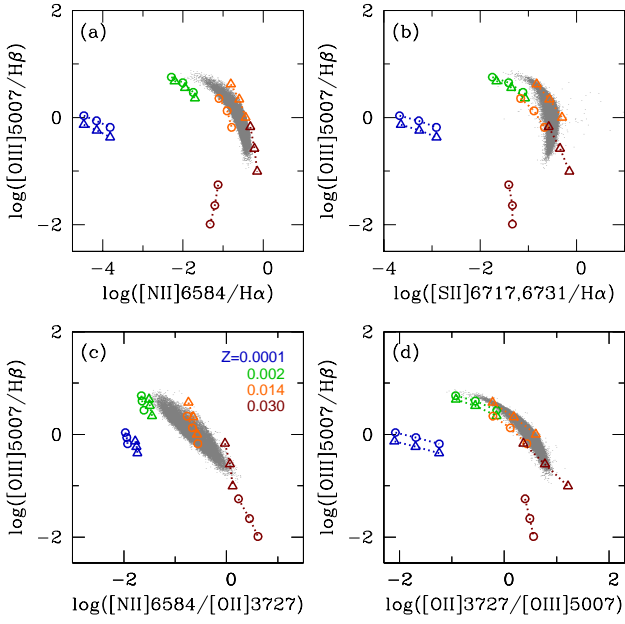


Figure 3. Same as Fig. 2, but for a subset of interstellar metallicities (colour-coded as indicated) and associated zero-age ionization parameters (using the dependence of U_S on Z_{ISM} identified by Carton et al., in preparation; see equation 4.2 of Chevallard & Charlot 2016): $Z_{ISM} = 0.0001$ for $\log U_S = -1.0, -1.5$ and -2.0 (in order of increasing $[O\text{ III}]/H\beta$ ratio and connected by a line); $Z_{ISM} = 0.002$ for $\log U_S = -2.0, -2.5$ and -3.0 ; $Z_{ISM} = 0.014$ for $\log U_S = -2.5, -3.0$ and -3.5 ; and $Z_{ISM} = 0.030$ for $\log U_S = -3.0, -3.5$ and -4.0 . In each panel, models are shown for two different dust-to-metal mass ratios, $\xi_d = 0.1$ (circles) and 0.5 (triangles).

(Figs 2a and 2c). We note that, because of our adoption of the same metallicity for the stars and the ISM, lowering Z_{ISM} also leads to a harder ionizing spectrum (since metal-poor stars evolve at higher effective temperatures than metal-rich ones; e.g., fig. 15 of Bressan et al. 2012). This has little influence on the results of Fig. 2, which are largely dominated by the other effects described above.

Zero-age ionization parameter at the Strömgren radius. Fig. 2 shows that increasing U_S at fixed other parameters makes the $[O\text{ III}]/H\beta$ ratio rise and the $[O\text{ II}]/[O\text{ III}]$, $[N\text{ II}]/H\alpha$ and $[S\text{ II}]/H\alpha$ ratios drop. This is because increasing U_S at fixed density n_H and ionizing photon rate $Q(0)$ in our model amounts to increasing the effective gas filling factor ϵ (equation 7 of Section 2.2), causing the $H\text{ II}$ regions to be more compact and concentrated close to the ionizing star clusters. This strengthens the high-ionization $[O\text{ III}]\lambda 5007$ line relative to the lower-ionization $[O\text{ II}]\lambda 3727$, $[N\text{ II}]\lambda 6584$ and $[S\text{ II}]\lambda\lambda 6717, 6731$ lines.

Dust-to-metal mass ratio. The effects of changes in ξ_d at fixed other parameters are shown in Fig. 3. For clarity, we plot models for only a subset of 4 interstellar metallicities and 3 associated zero-age ionization parameters (using the dependence of U_S on Z_{ISM} identified by Carton et al., in preparation; see equation 4.2 of Chevallard & Charlot 2016). Increasing ξ_d depletes metal coolants from the gas phase. The electronic temperature increases, as does cooling through collisionally excited optical transitions (e.g. Shields & Kennicutt 1995). The implied rise in $[N\text{ II}]/H\alpha$ and $[S\text{ II}]/H\alpha$ ratios is significantly stronger than that in

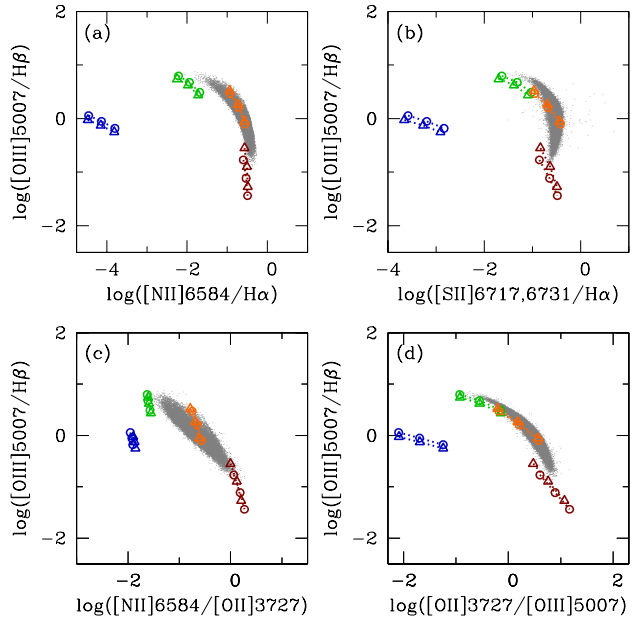


Figure 4. Same as Fig. 3, but for models with two different carbon-to-oxygen ratios, $C/O = 0.1$ (circles) and 1.4 (triangles) times $(C/O)_\odot$.

$[O\text{ III}]/H\beta$ ratio (Figs 3a and 3b), because oxygen is a refractory element strongly depleted from the gas-phase (making the $[O\text{ III}]/H\beta$ ratio drop as ξ_d increases), while S and N are both non-refractory elements (Table 1). Fig. 3 further shows that, not surprisingly, the effect changing ξ_d is more pronounced at high than at low Z_{ISM} .

Carbon-to-oxygen abundance ratio. In our model, increasing the C/O ratio at fixed other parameters amounts to increasing the abundance of carbon and decreasing the abundances of all other heavy elements to maintain the same Z_{ISM} (Section 2.3.1). As Fig. 4 shows, therefore, the effect of raising the C/O ratio on emission-line ratios involving N, O and S transitions is similar to that of lowering the interstellar metallicity Z_{ISM} (shown by the solid line in Fig. 2).

Hydrogen gas density. A rise in n_H increases the probability of an excited atom to be de-excited collisionally rather than radiatively. Since the critical density for collisional de-excitation is lower for infrared fine-structure transitions than for optical transitions, the net effect of raising n_H at fixed other parameters is to reduce the cooling efficiency through infrared transitions and increase that through optical transitions. Fig. 5 shows that the implied rise in the $[O\text{ III}]/H\beta$, $[N\text{ II}]/H\alpha$ and $[S\text{ II}]/H\alpha$ ratios is small at low metallicity, but much stronger at high metallicity, where infrared fine-structure transitions dominate the cooling (e.g., Oey & Kennicutt 1993, see also the discussion of Fig. 2 above).

Upper mass cutoff of the IMF. Increasing m_{up} from 100 to $300 M_\odot$ makes the ionizing spectrum of the stellar population harder, since stars with initial masses greater than $100 M_\odot$ evolve at higher effective temperatures than lower-mass stars. As Fig. 6 shows, this makes the high-ionization lines stronger, causing a rise of the $[O\text{ III}]/H\beta$ ratio – and to a lesser extent, the $[N\text{ II}]/H\alpha$ and $[S\text{ II}]/H\alpha$ ratios – and a drop of the $[O\text{ II}]/[O\text{ III}]$ ratio.

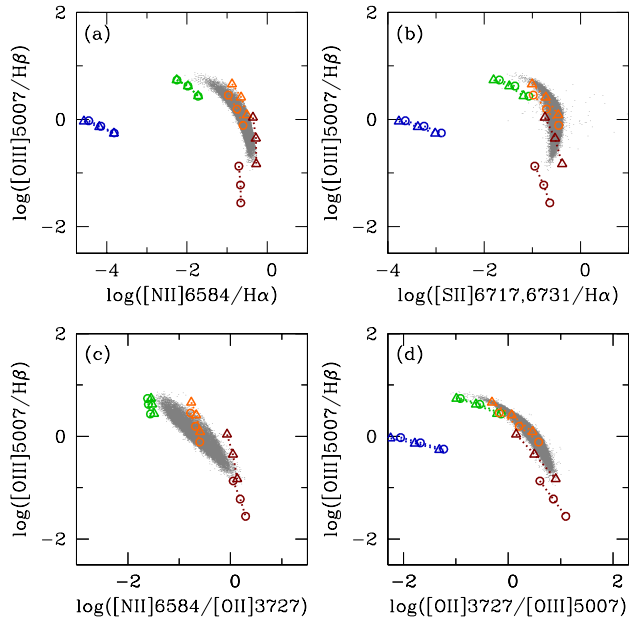


Figure 5. Same as Fig. 3, but for models with two different hydrogen densities, $n_{\text{H}} = 10 \text{ cm}^{-3}$ (circles) and 10^3 cm^{-3} (triangles).

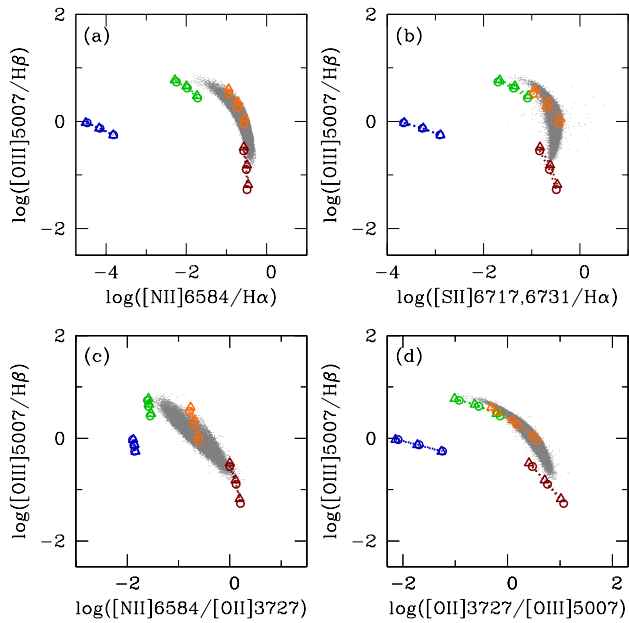


Figure 6. Same as Fig. 3, but for models with two different IMF upper mass cutoffs, $m_{\text{up}} = 100 M_{\odot}$ (circles) and $300 M_{\odot}$ (triangles).

Hence, the various adjustable parameters of the model of nebular emission described in Section 2 influence, each in its own way, the optical emission-line spectra of star-forming galaxies. These specific signatures enable one to constrain simultaneously, in return, the star-formation and interstellar-gas parameters of observed galaxies with measured optical emission-line intensities (see, e.g., CL01; Brinchmann et al. 2004; Pacifici et al. 2012). As mentioned previously, a main

originality (other than the use of updated stellar population and photoionization prescriptions) of the models presented in Figs 2–6 above relative to previous models of the optical nebular emission from star-forming galaxies lies in the versatile, yet self-consistent, accounting of gas-phase versus interstellar element abundances, which allows investigations of chemically young galaxies with non-scaled solar element abundance ratios.

4 ULTRAVIOLET EMISSION-LINE PROPERTIES

One of our primary motivations in this work is to build a library of photoionization models useful to interpret observations of the rest-frame ultraviolet emission from young star-forming galaxies at high redshifts. In this section, we investigate the ultraviolet properties of the grid of models presented in the previous sections and compare these predictions with available observations of a small, heterogeneous sample of local and distant star-forming galaxies. For illustration purposes, we have selected – by means of a systematic investigation by eye of ratios involving the strongest ultraviolet emission lines – a set of emission-line ratios most sensitive to changes in the adjustable parameters of our model. These ratios involve six emission lines (or multiplets) commonly detected in the spectra of star-forming galaxies: $\text{N V } \lambda\lambda 1238, 1242$ (hereafter $\text{N V } \lambda 1240$); $\text{C IV } \lambda\lambda 1548, 1551$ (hereafter $\text{C IV } \lambda 1550$); $\text{He II } \lambda 1640$; $\text{O III } \lambda 1666$; $[\text{Si III}] \lambda 1883 + [\text{Si III}] \lambda 1892$ (hereafter $[\text{Si III}] \lambda 1888$); and $[\text{C III}] \lambda 1907 + [\text{C III}] \lambda 1909$ (hereafter $[\text{C III}] \lambda 1908$). We note that, while the luminosities of $\text{O III } \lambda 1666$, $[\text{Si III}] \lambda 1888$ and $[\text{C III}] \lambda 1908$ can usually be measured in a straightforward way when these lines are detectable, measurements of nebular $\text{He II } \lambda 1640$ may be challenged by the presence of a broad component arising from Wolf-Rayet stars, especially at metallicities $Z_{\text{ISM}} \gtrsim 0.006$ (because of both a drop in photons capable of producing nebular $\text{He II } \lambda 1640$ and a rise in stellar $\text{He II } \lambda 1640$ emission as metallicity increases; e.g. Schaefer & Vacca 1998). At such metallicities, measurements of nebular $\text{N V } \lambda 1240$ and $\text{C IV } \lambda 1550$ are even more challenging, because of the contamination by strong P-Cygni absorption features from O-star winds (Walborn & Panek 1984) coupled with interstellar absorption (see Vidal-García et al., in preparation, for a detailed modelling of these competing effects).

Fig. 7 shows the ultraviolet properties of the same set of photoionization models (extracted from the grid of Table 3) as that for which we showed the optical properties in Fig. 2. Also shown in grey in the top-left panel of Fig. 7 are measurements of the $[\text{C III}] / [\text{O III}]$ and $[\text{Si III}] / [\text{C III}]$ ratios in the spectra of six giant extragalactic H II regions in nearby low-luminosity, metal-poor, dwarf irregular galaxies observed with the *Hubble Space Telescope*/Faint Object Spectrograph (*HST*/FOS; from Garnett et al. 1995). In the top two panels, the red data points show measurements of (and limits on) the $[\text{C III}] / [\text{O III}]$, $[\text{Si III}] / [\text{C III}]$, $\text{He II} / [\text{O III}]$ and $\text{C IV} / [\text{C III}]$ ratios in the spectra of four low-mass, gravitationally-lensed dwarf galaxies at redshift in the range $2 \lesssim z \lesssim 3$ observed with the Keck low-resolution imaging spectrometer (LRIS) and Very Large Telescope Focal Reducer and Low Dispersion Spectrograph (VLT FORS2; from Stark et al. 2014). The model grid

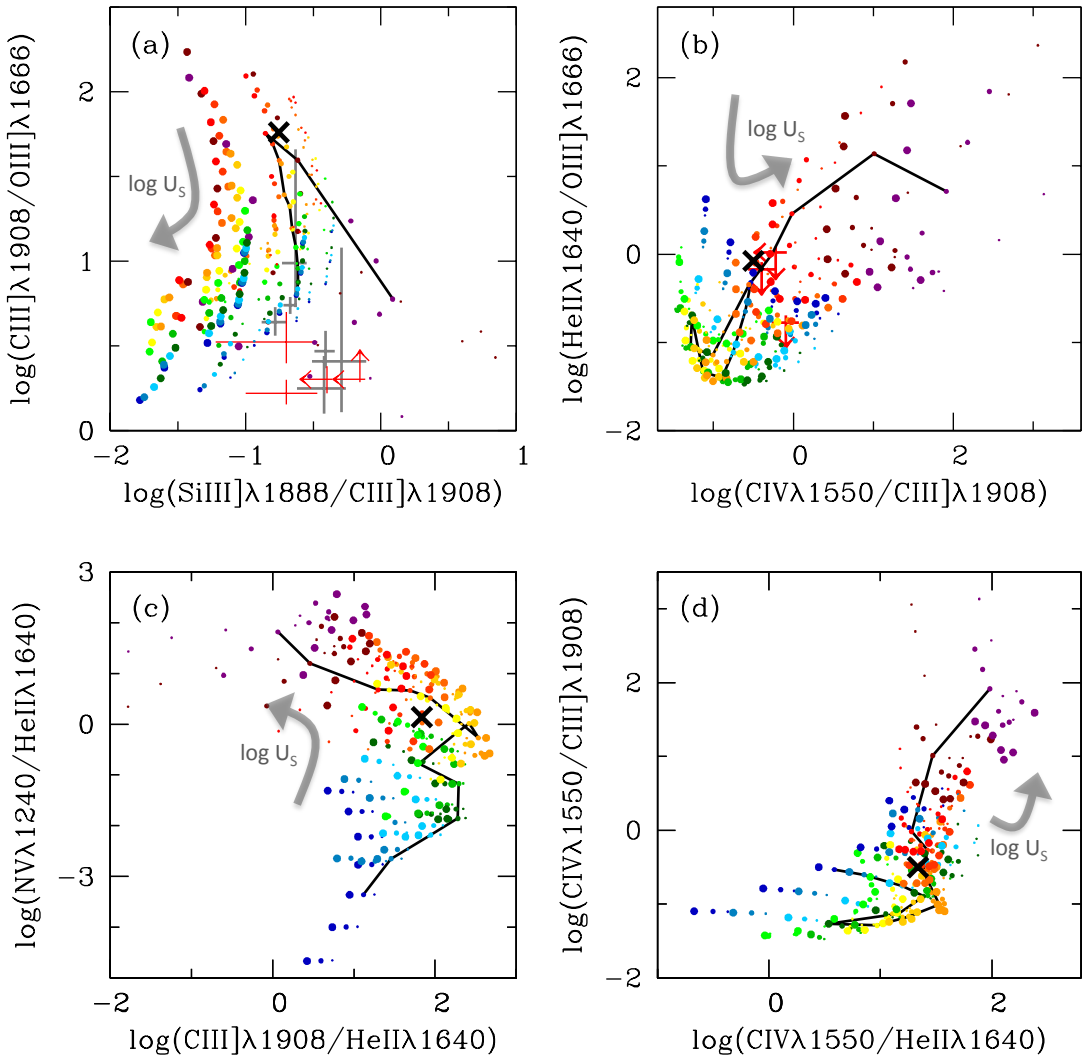


Figure 7. Luminosity ratios of prominent ultraviolet emission lines predicted by the photoionization models described in Section 2: (a) $\text{CIII}] \lambda 1908 / \text{OIII}] \lambda 1666$ against $\text{SiIII}] \lambda 1888 / \text{CIII}] \lambda 1908$; (b) $\text{HeII} \lambda 1640 / \text{OIII}] \lambda 1666$ against $\text{CIV} \lambda 1550 / \text{CIII}] \lambda 1908$; (c) $\text{Nv} \lambda 1240 / \text{HeII} \lambda 1640$ against $\text{CIII}] \lambda 1908 / \text{HeII} \lambda 1640$; and (d) $\text{CIV} \lambda 1550 / \text{CIII}] \lambda 1908$ against $\text{CIV} \lambda 1550 / \text{HeII} \lambda 1640$. In each panel, the models and solid line are the same as in Fig. 2. In panel (a), the grey and red crosses refer to observations (including error bars and upper limits) of, respectively, six giant extragalactic H II regions in nearby low-luminosity, metal-poor, dwarf irregular galaxies observed with *HST*/FOS by Garnett et al. (1995) and four low-mass, gravitationally-lensed dwarf galaxies at redshift in the range $2 \lesssim z \lesssim 3$ observed with Keck/LRIS and VLT/FORS2 by Stark et al. (2014, also reported in panel b).

encompasses the few observational measurements in Fig. 7. In fact, the models presented here have already been used successfully to interpret rest-frame ultraviolet observations of the nebular emission from young star-forming galaxies at high redshifts (Stark et al. 2014, 2015a,b, 2016).

We now explore the influence of the main adjustable parameters of our model on the predicted emission-line properties of star-forming galaxies in these four ultraviolet diagnostics diagrams. As in Section 3.3 above, we describe the effect of varying a single parameter at a time, keeping the other main adjustable parameters fixed:

Interstellar metallicity. Globally, the effect of increasing Z_{ISM} at fixed other parameters, shown by the solid line in Fig. 7, can be understood in terms of the balance pointed out in Section 3.3 (Fig. 2) between the implied rise in the abundance

of coolants, associated drop in electronic temperature and cooling through infrared fine-structure transitions. As a result, ratios of metal-line to $\text{HeII} \lambda 1640$ luminosities tend to rise, stagnate and eventually drop again when metallicity increases in Fig. 7, while the inclusion of secondary nitrogen production causes the Nv/HeII ratio to rise steadily with Z_{ISM} (Fig. 7c).

Zero-age ionization parameter at the Strömgren radius. In our model, increasing U_S at fixed other adjustable parameters causes the H II regions to be more compact and concentrated close to the ionizing star clusters (Section 3.3). Overall, this makes the luminosity ratios of lines with highest ionization potential to lines with lower ionization potential (such as the inverse of the $\text{CIII}] / \text{OIII}]$ ratio plotted in Fig. 7a and the $\text{CIV}/\text{CIII}]$ ratio) and the $\text{HeII} \lambda 1640$ line (such as the CIV/HeII and Nv/HeII ratios) rise in Fig. 7 (see fig. 1 of

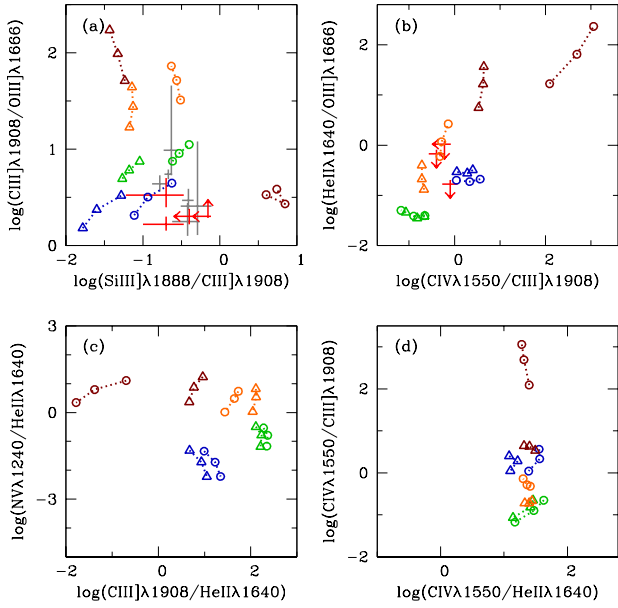


Figure 8. Same as Fig. 7, but for the same subset of interstellar metallicities and associated zero-age ionization parameters as in Fig. 3. In each panel, models are shown for two different dust-to-metal mass ratios, $\xi_d = 0.1$ (circles) and 0.5 (triangles).

Feltre et al. 2016 for a graphical summary of the ionization potentials of the different species considered in Fig. 7).

Dust-to-metal mass ratio. Fig. 8 illustrates the influence of ξ_d on the predicted ultraviolet emission-line ratios, showing for clarity only models for the same subset of Z_{ISM} and U_S combinations as used in Fig. 3 above. As for optical transitions (Section 3.3), the response of ultraviolet transitions to a rise in ξ_d results from a balance between the implied depletion of coolants from the gas phase, the associated rise in electronic temperature and the relative depletions of different species (Table 1). For example, the C III]/He II and C IV/He II ratios drop at low Z_{ISM} as ξ_d rises, because of the disappearance of C from the gas phase, but the trend is opposite at high Z_{ISM} , because the rise in electronic temperature induced by the depletion of heavy elements is more significant (Figs 8c and 8d). In Fig. 8a, the Si III]/C III] drops at all metallicities when ξ_d rises, because Si is far more depleted than C from the gas phase. In contrast, since N is not depleted, the N V/He II ratio shows only a mild increase as ξ_d rises in Figs 8c, because of the rise in electronic temperature. We note that, at high metallicity especially, the increase in dust optical depth ($\tau_d \propto \xi_d Z_{\text{ISM}} n_{\text{He}}$) induced by a rise in ξ_d makes the electronic temperature drop through the enhanced absorption of energetic photons, causing the C IV/C III] and C IV/He II ratios to drop and the C III]/O III] ratio to rise.

Carbon-to-oxygen abundance ratio. Increasing the C/O ratio at fixed other parameters consists in increasing the abundance of C while decreasing those of all other heavy elements (Section 3.3). Fig. 9 shows that, as a result, raising the C/O ratio makes the C III]/O III], C III]/He II and C IV/He II ratios markedly larger and the Si III]/C III] ratio markedly smaller. Another important conclusion we can draw from this figure is that the presence of the C III]λ1908, C IVλ1550 and O III]λ1663 emission lines at ultraviolet wave-

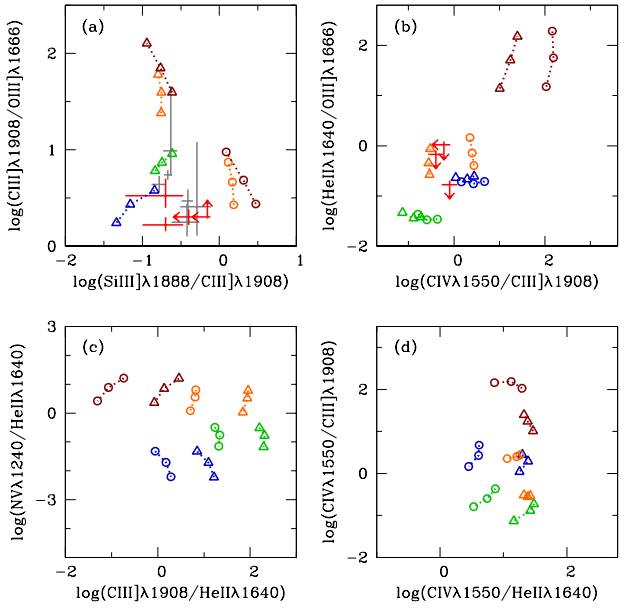


Figure 9. Same as Fig. 8, but for models with two different carbon-to-oxygen ratios, $C/O = 0.1$ (circles) and 1.4 (triangles) times $(C/O)_\odot$.

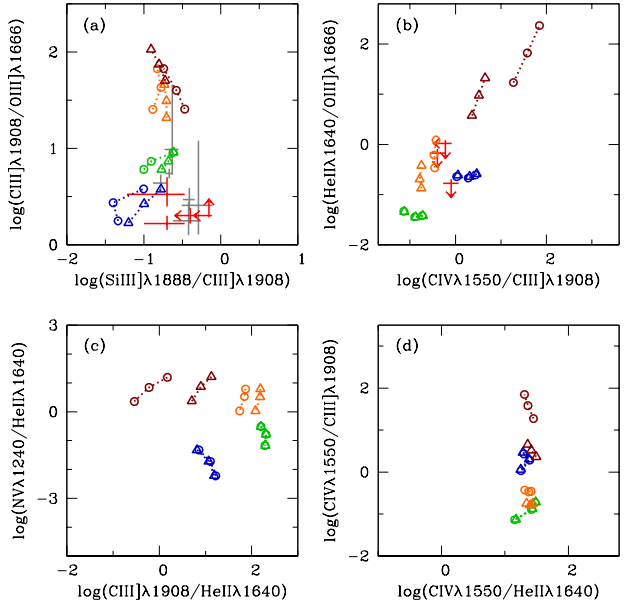


Figure 10. Same as Fig. 8, but for models with two different hydrogen densities, $n_{\text{H}} = 10 \text{ cm}^{-3}$ (circles) and 10^3 cm^{-3} (triangles).

lengths makes ultraviolet-line ratios more direct tracers of the C/O ratio of young star-forming galaxies than the standard optical emission lines investigated in Fig. 4.

Hydrogen gas density. The effect of raising n_{H} at fixed other parameters is to increase radiative cooling through ultraviolet and optical transitions relative to infrared ones (Section 3.3). As Fig. 10 shows, this makes the C III]/He II and C IV/He II ratios rise and the He II/O III] ratio drop. Also, in our model, increasing n_{H} at fixed other parame-

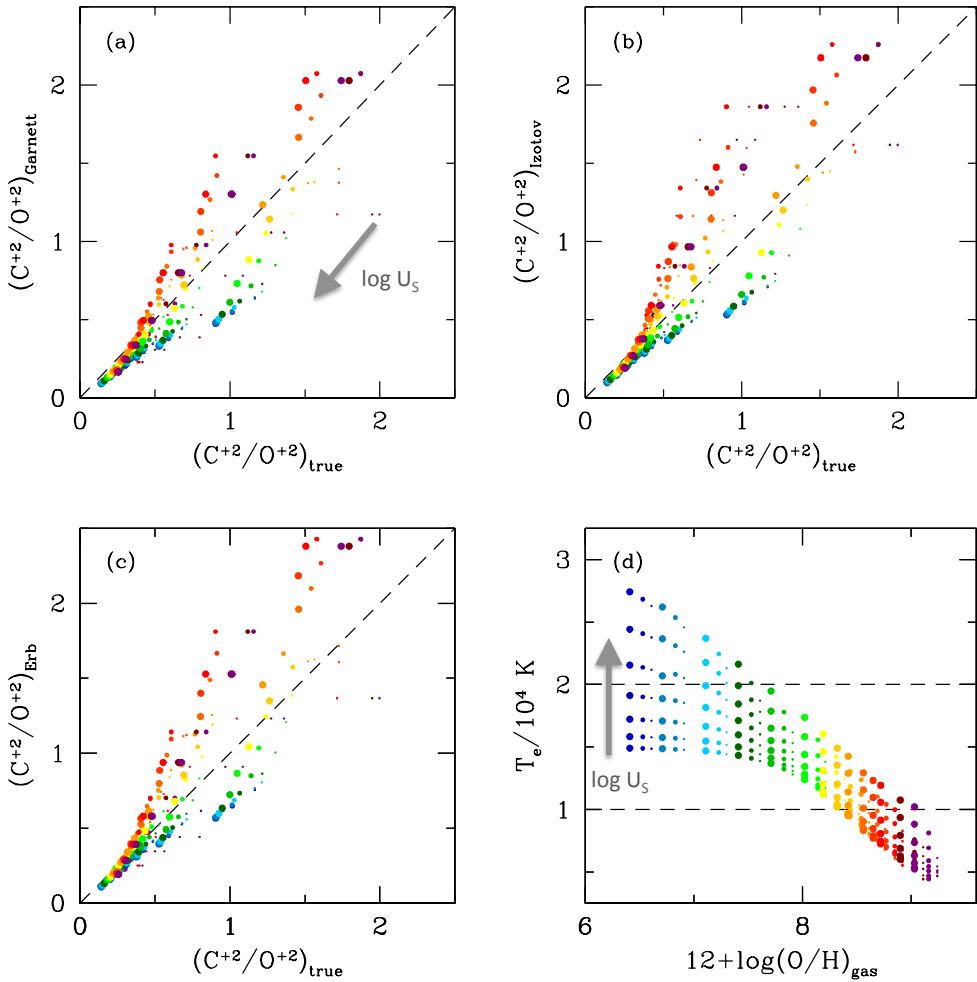


Figure 12. C⁺²/O⁺² ionic abundance ratio estimated from emission-line luminosities via standard formulae involving the direct- T_e method plotted against true C⁺²/O⁺² ratio, for the same models as in Fig. 2: (a) according the prescription of Garnett et al. (1995, equation 15 of Section 5.2); (b) according the prescription of Izotov & Thuan (1999, equation 16); (c) according the prescription of Erb et al. (2010, equation 14). (d) Model electronic temperature in the O⁺² plotted against gas-phase oxygen abundance for the same models as in panels (a)–(c). Dashed horizontal lines bracket the approximate T_e range over which equations (15)–(17) were calibrated (see text for details).

lower ionization potential of C⁺² (47.9 eV) relative to O⁺² (54.9 eV) implies that $X(C^{+2})$ starts to drop before $X(O^{+2})$, because of the ionization of C to C⁺³, causing the ICF to also increase. Also shown for comparison in Fig. 13a are the pioneer, dust-free calculations of the ICF by Garnett et al. (1995) for OB stellar associations at ages $t' = 0$ and 2 Myr (in the notation of Section 2.2), based on early prescriptions by Mihalas (1972) and Panagia (1973). These calculations for large $X(O^{+2})$ are in reasonable agreement with our more sophisticated models of H II-region populations in star-forming galaxies.

It is important to note that, although the scatter in the ICF predicted at fixed $X(O^{+2})$ by our models is moderate in Fig. 13a, the influence of this scatter on estimates of the (C/O)_{gas} ratio via equation (14) is amplified by the uncertainties affecting observational estimates of $X(O^{+2})$ from ratios of oxygen emission lines through the direct- T_e method (Section 5.1). To show this, we make the standard approximation that the fraction of doubly-ionized oxygen can be

estimated as

$$X(O^{+2}) \approx \frac{O^{+2}/H^+}{O^+/H^+ + O^{+2}/H^+}, \quad (20)$$

i.e., we neglect the contributions by O⁰ and O³⁺ to the total oxygen abundance. These contributions are expected to be significant only in the cases of, respectively, very low and very high ionization parameter (e.g. Kobulnicky et al. 1999; Izotov et al. 2006). We adopt the prescription of Izotov et al. (2006, their equations 3 and 5) to compute the abundances of O⁺ and O⁺² in equation (20) from observed emission-line luminosities, i.e.,

$$\log O^+/H^+ = \log \frac{L([O\,\mathrm{II}]\lambda 3727)}{L(H\beta)} - 6.039 + \frac{1.676}{t_e} - 0.40 \log t_e - 0.034 t_e + \log(1 + 1.35x) \quad (21)$$

- Stark, D. P., Ellis, R. E., Charlot, S., et al. 2016, [\(arXiv:1606.01304\)](https://arxiv.org/abs/1606.01304)
- Stasińska, G. 1980, A&A, 85, 359
- Stasińska, G. 2005, A&A, 434, 507
- Stasińska, G., & Leitherer, C. 1996, ApJS, 107, 661
- Steidel, C. C., Rudie, G. C., Strom, A. L., et al. 2014, ApJ, 795, 165
- Steidel, C. C., Strom, A. L., Pettini, M., et al. 2016, [\(arXiv:1605.07186\)](https://arxiv.org/abs/1605.07186)
- Stoughton, C., Lupton, R. H., Bernardi, M., et al. 2002, AJ, 123, 485
- Todt, H. and Sander, A. and Hainich, R., et al. 2015, A&A, 579, A75
- Tremonti, C. A., Heckman, T. M., Kauffmann, G., et al. 2004, ApJ, 613, 898
- van den Hoek, L. B., & Groenewegen, M. A. T. 1977, A&AS, 123, 305
- Veilleux, S., & Osterbrock, D. E. 1987, ApJS, 63, 295
- Villar-Martín, M., Cerviño, M., & González Delgado, R. M. 2004, MNRAS, 355, 1132
- Walborn, N. R. and Panek, R. J. 1984, ApJ, 286, 718
- Wang, J., Heckman, T. M., & Lehnert, M. D. 1997, ApJ, 491, 114
- Willott, C. J., Delorme, P., Reylé, C., et al. 2010, AJ, 139, 906
- Wofford, A. and Charlot, S. and Bruzual, G., et al. 2016, MNRAS, 457, 4296
- Zackrisson, E., Bergvall, N., Olofsson, K., & Siebert, A. 2001, A&A, 375, 814

This paper has been typeset from a TeX/LaTeX file prepared by the author.